

Rapid Vibrational Circular Dichroism Spectroscopy via Synchronized Photoelastic Modulator-Quantum Cascade Laser Integration

Viviana Arrunategui Norvick, Michael Le, Eric Modesitt, Owen Myers, Roya Akrami, and Yamuna Phal*



Cite This: *ACS Meas. Sci. Au* 2025, 5, 729–739



Read Online

ACCESS |

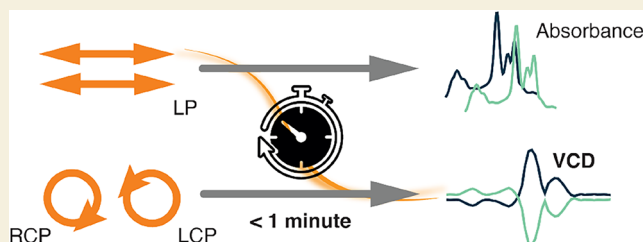
Metrics & More

Article Recommendations

Supporting Information

ABSTRACT: Accurate and rapid analysis of chirality is crucial for understanding biological processes and molecular interactions, yet traditional vibrational circular dichroism (VCD) techniques are limited by long acquisition times and low throughput. We present a quantum cascade laser (QCL)-based VCD system that integrates a photoelastic modulator (PEM) with pulsed laser sources, using precise temporal synchronization and a novel calibration method based on Welch's power spectral density analysis. This hardware-software integration enables real-time demodulation without the need for conventional lock-in amplifiers and achieves accurate, high-SNR VCD spectra of α -pinene (\pm) mixtures with high reproducibility. Real-time enantiomeric excess determination is achieved with a 10 \times improvement in speed and a 5 \times enhancement in SNR compared to conventional VCD methods. These advancements pave the way for high-throughput and nondestructive chiral analysis, with potential applications in biosensing, structural biology, and pharmaceutical research.

KEYWORDS: quantum cascade laser, vibrational circular dichroism, photoelastic modulator, chirality detection, enantiomeric excess, mid-infrared, chiral molecule characterization



Absorbance
 VCD
 RCP LCP LP < 1 minute

INTRODUCTION

Chirality is a geometric property that manifests across scales, and in molecular systems, it plays a pivotal role in biological processes. For example, amino acids found in proteins are predominantly in the left-handed (L) configuration, while naturally occurring sugars, including those associated with DNA exhibit a right-handed (D) form. These configurational differences are critical in biological activities such as metabolic and regulatory processes, particularly in drug-cell interactions where molecular recognition requires high spatial and temporal specificity. Proteins often exhibit strong binding preferences for a single stereoisomer, and even trace amounts of the nontarget enantiomer can lead to unintended, sometimes severe, side effects.^{1–3} Consequently, precise stereoselective synthesis, characterization, and separation of chiral compounds are essential in fields such as pharmaceutical development^{1,4,5} and biosensing.^{5,6}

Optical techniques like vibrational circular dichroism (VCD)^{7–11} and Raman optical activity (ROA) offer unique capabilities for studying molecular chirality by exploiting differences in the interaction of circularly polarized light with chiral molecules. Among these, VCD spectroscopy^{12–16}—measuring the differential absorption of left- and right-circularly polarized infrared (IR) light—stands out due to its ability to analyze chiral molecules without requiring chemical modifications or additional reagents. Complementing the instrumentation development from dispersive to Fourier transform infrared (FT-IR) instruments, previous studies

have demonstrated the utility of density functional theory (DFT) in predicting vibrational circular dichroism (VCD) spectra, enabling detailed comparisons between experimental results and theoretical models to elucidate the underlying chiral vibrational modes.^{17–20} The integration of experimental VCD with DFT calculations provides a powerful approach for validating chiroptical measurements and understanding molecular chirality. This makes VCD particularly useful for applications such as assessing racemic mixtures, protein secondary structure determination,^{11,21–27} and reaction monitoring in asymmetric synthesis.^{10,16,28,29} While traditional VCD instruments based on FT-IR technology provide high throughput and multiplexing capabilities, they suffer from long acquisition times, often requiring 30 min to several hours to achieve adequate signal-to-noise ratio (SNR).³⁰

Recent advances in quantum cascade lasers (QCLs) offer promising alternatives for VCD spectroscopy^{31–34} by providing high brilliance and tunability of laser sources in the mid-IR region.^{35,36} However, integrating QCLs with photoelastic modulators (PEMs)—essential components for dynamic polarization modulation—presents new challenges, particularly in

Received: June 9, 2025

Revised: August 13, 2025

Accepted: August 14, 2025

Published: August 20, 2025



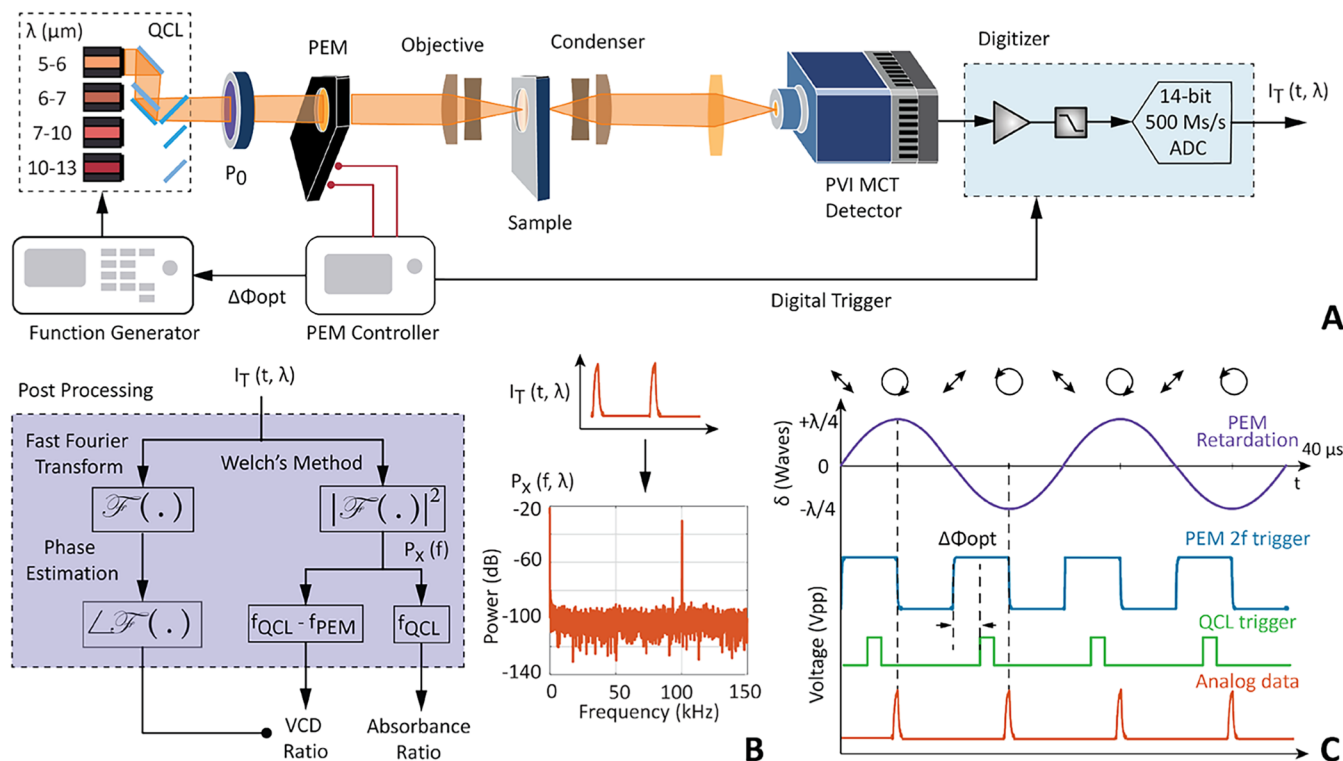


Figure 1. (A) Optical schematic of QCL-based VCD spectrometer includes the following components: QCL = quantum cascade laser; PEM = photoelastic modulator (an electrically switched wavelength-tunable quarter wave plate); P_0 = polarizer and PVI MCT = photovoltaic mercury cadmium telluride detector. Back-end data acquisition and control system uses a high-speed digitizer card (DAQ) card to capture and process the amplitude modulated signal acquired by a detector. (B) Postprocessing workflow for extracting frequency components from time-series data, $I_T(t, \lambda)$. Welch's method is applied to the time series data, $I_T(t, \lambda)$, to extract the f_{QCL} and $f_{QCL} - f_{PEM}$ frequency components. The method involves splitting the time signal into overlapping segments, applying a window function to each segment, and calculating the periodogram $P_x(f, \lambda)$ from the time-series data $I_T(t, \lambda)$. Inset plot shows Power spectral density (PSD) visualization, highlighting the identified frequency components, ensuring accurate signal demodulation and noise reduction for reliable VCD signal extraction. (C) Time series plots showing PEM retardance and associated light polarization states, PEM trigger signal, calibrated QCL trigger signal with phase shift $\Delta\Phi_{opt}$, and data with laser pulses triggered by the QCL trigger. There is a small, deterministic delay between the QCL trigger signal and the actual laser emission.

maintaining synchronization between the pulsed laser source and the modulator. Also, instead of retrofitting existing mid-IR imaging platforms for acquiring VCD spectral measurements, alongside absorbance measurements,³¹ our proposed innovation instead focuses on developing a QCL-VCD spectrometer system from first design principles, i.e., generation of purely CP light states. PEMs are widely used in circular dichroism (CD) and VCD systems for their ability to dynamically modulate retardance with high precision. Unlike Kerr and Pockels cells, PEMs operate with isotropic materials and provide stable modulation across a wide wavelength range, making them particularly suitable for QCL-based systems.^{37,38} However, achieving the temporal precision necessary for high-speed VCD measurements requires advanced synchronization and calibration strategies.

In this work, we address the limitations of traditional and prior VCD methods by presenting a novel QCL-based VCD system with subminute acquisition times. Furthermore, we investigate critical design elements for achieving high-accuracy QCL-VCD systems, addressing previously overlooked aspects such as the integration of PEMs with pulsed-laser sources, the selection of polarization-insensitive detectors, and the implementation of low-NA optics to enhance signal collection. Our approach combines an optimized calibration method using Welch's power spectral density analysis for enhanced retardance accuracy with a novel synchronization strategy for

integrating PEMs and pulsed QCLs. We demonstrate the system's ability to perform real-time enantiomeric excess measurement of α -pinene (\pm) mixtures and report precise retardance calibration across the 5.7–10 μm wavelength range. Furthermore, we show that our lock-in-free detection system achieves more than a 10 \times improvement in acquisition speed and a 5 \times enhancement in spectral SNR compared to traditional techniques. These advancements enable rapid, nondestructive chiral analysis, paving the way for expanded applications in biosensing and molecular spectroscopy.

EXPERIMENTAL SECTION

Optical Setup

The experimental setup of our proposed subminute QCL-VCD spectrometer is illustrated in Figure 1A. The setup consists of a tunable quantum cascade laser (LaserTune Block Engineering QCL), a polarizer (WP25H-Z ZnSe Holographic Wire Grid Polarizer), a photoelastic modulator (PEM 200 IIIZS50, Hinds Instruments), and a mercury cadmium telluride (MCT) photodetector (Vigo Systems MCT PVI-4TE). The signal is focused using a ZnSe-ZnS air-spaced achromatic doublet lens (AC254-050-E3, ARC: 7–12 μm , $f = 50$ mm). The QCL emits vertically polarized light between 5 and 13 μm in pulse operation up to 2 MHz with 6% duty cycle. The linear polarizer is aligned to the QCL's polarization at 0° to the vertical axis. The PEM is modulated at 50 kHz, with its phase varying sinusoidally between $\pm\alpha_0$, the initial uncalibrated phase. The PEM's fast optical axis is oriented at 45° relative to the input polarization and is slightly

angled toward the beam to reduce back reflections and interference at the detector. The PEM is modulated by an external controller that transmits a trigger signal to a waveform generator. The timing and control diagram is shown in Figure 1B. The process to determine optimum time delay, $\Delta\Phi_{\text{opt}}$, is directly related to the PEM calibration and is described in the **Results and Discussion** section. The waveform generator then creates a new trigger signal for the QCL, effectively compensating for any time delays between the PEM and the laser. The light is then directed to the MCT photodetector, and the signal is sent to a digitizer for data acquisition and postprocessing.

Software and Data Acquisition

To efficiently manage the experimental setup and ensure precise control over the data acquisition process, custom software scripts were developed using Python. These scripts automate the initialization, configuration, and operation of all laboratory devices involved in the experiment, including the Quantum Cascade Laser (QCL), the Photoelastic Modulator (PEM), the motorized polarizers, the signal generator, and the high-speed digitizer. The automation software interfaces with the devices using appropriate communication protocols. The QCL is controlled via a TCP/IP interface, allowing for remote tuning of the laser's wavenumber. The PEM controller communicates over a serial interface to adjust retardance settings dynamically. The front and back polarizers are mounted on motorized rotation stages from Thorlabs, which are controlled via USB connections using the Kinesis API. The signal generator and digitizer are accessed using standard instrument communication protocols (SCPI), enabling precise timing and synchronization. The software begins by initializing all devices and setting them to their default states. The polarizers are homed and moved to their starting positions, with the back polarizer typically set to achieve cross-polarization relative to the front polarizer. The signal generator is configured to produce trigger signals that synchronize the PEM modulation with the laser pulses. By adjusting the delay settings on the signal generator, any phase differences between the PEM and the laser pulses are compensated for, ensuring proper synchronization. Data acquisition is performed using a high-speed digitizer (Spectrum M4i series), which is configured to capture waveform data synchronously with the PEM modulation and laser pulses. The digitizer operates in multiple recording mode, capturing a specified number of samples per segment at a high sample rate (e.g., 500 MHz). Trigger settings are configured to ensure that data acquisition begins precisely when the laser pulses and PEM modulation are aligned. The automation script systematically loops over a predefined list of wavenumbers and retardance values, enabling comprehensive data collection across the experimental parameter space.

First, the QCL is tuned to the desired wavelength using software control, enabling the study of PEM behavior at specific wavelengths corresponding to laser emission. The PEM's retardance amplitude is then configured to match the current wavenumber, ensuring proper calibration for the selected laser wavenumber. Data acquisition is initiated via software, with built-in error-handling mechanisms to address potential issues such as timeouts or communication errors. The digitizer captures waveform data for the configured parameters, and the acquired data is saved as CSV files with naming conventions that include details such as wavenumber and retardance value, facilitating efficient retrieval and analysis. After data acquisition, the devices are reset or reconfigured to prepare for the next set of experimental parameters. The automation scripts employed in this workflow are designed with robust error handling and logging capabilities. These scripts ensure that any issues are promptly identified and addressed without disrupting the entire experiment. Transient errors are managed with retries and delays, while detailed logs of events and parameters provide a comprehensive record of the experimental process for analysis and troubleshooting.

Post-Processing

Next, we outline the essential data processing steps necessary to derive the VCD spectra, as illustrated in Figure 1C. While the DC and f_{PEM} components are essential for acquiring absorbance and VCD measurements in traditional FT-IR spectrometers, in pulsed-laser-

based VCD spectrometers, the dominant frequencies shift to f_{QCL} and $f_{\text{QCL}} - f_{\text{PEM}}$.³¹ Traditionally, lock-in amplifiers have been employed to extract these frequency components, but we utilize time-domain gating and Welch's method as a superior alternative due to its efficiency in extracting frequency components from noisy time-domain signals.

Traditional lock-in amplifiers (LIAs) extract signals by multiplying the input with a reference sinusoid and integrating over a full period. While effective for continuous or symmetric signals with duty cycles above 50%, their performance degrades significantly with low duty cycle signals. In our system, the QCL operates with 60 ns pulses synchronized to the $2f$ component of a 50 kHz PEM, effectively sampling at 100 kHz to capture both the crest and the trough retardance states, resulting in a duty cycle of just 0.6%. Under these conditions, the SNR becomes heavily dependent on internal amplification and filtering, reducing the efficiency of conventional LIA-based detection. To address the low-duty cycle, we implement time gating during postprocessing to isolate signal components within the narrow pulse window, thereby minimizing noise contributions before further analysis.

Although LIAs remain prevalent in signal detection, direct data acquisition combined with Fourier-based analysis has demonstrated comparable or superior performance in various applications,^{39,40} including spectroscopy and biomedical sensing.^{41,42} For our application, Welch's method for power spectral density (PSD) estimation offers improved robustness over standard Fourier analysis and lock-in amplifiers. Unlike traditional LIA methods that rely on analog phase-sensitive detection and are prone to low-frequency noise and baseline drift, Welch's method offers superior flexibility and digital resolution.^{43,44} Welch's method reduces variance in PSD estimates by dividing the time-domain signal into overlapping segments, applying a window function (Hann or Hamming), computing individual periodograms, and averaging them to suppress baseline noise.⁴⁵ While Welch's method involves additional signal processing, it is implemented using fast Fourier transforms (FFTs) and is computationally efficient, especially with modern DAQ hardware and open-source libraries (e.g., SciPy, MATLAB DSP toolbox). This adaptability makes Welch's method particularly well-suited for the dynamic nature of pulsed-laser-based VCD systems. The m th segment of the signal $x(n)$ is given by eq 1 where $w(n)$ is the window function, M is the segment length, R is the segment offset, K is the total number of segments, and where the symbol, \triangleq , is used to denote equal by definition.

$$x_m(n) \triangleq w(n)x(n + mR), \\ n = 0, 1, \dots, M - 1, m = 0, 1, \dots, K - 1 \quad (1)$$

The periodogram of the m th block, $P_{x_m, M}$ is given by eq 2, and the PSD based on the Welch's method, \hat{S}_x^W , is given by eq 3.⁴⁵

$$P_{x_m, M}(\omega_k) = \frac{1}{M} |\text{FFT}_{N, k}(x_m)|^2 \triangleq \frac{1}{M} \left| \sum_{n=0}^{N-1} x_m(n) e^{-j2\pi nk/N} \right|^2 \quad (2)$$

$$\hat{S}_x^W(\omega_k) \triangleq \frac{1}{K} \sum_{m=0}^{K-1} P_{x_m, M}(\omega_k) \quad (3)$$

The total power within a specific frequency band, ω_1 and ω_2 , can be approximated using eq 4 where $\Delta\omega$ is the frequency resolution. This total power can also serve as an approximation for the power associated with specific frequencies such as the f_{QCL} and $f_{\text{QCL}} - f_{\text{PEM}}$ signals of the measured data. The estimation accuracy depends on the window function and the length of the data segments used in the PSD calculation, which influence spectral leakage and frequency resolution.

$$P_{\text{band}} \approx \sum_{k=\omega_1}^{\omega_2} \hat{S}_x^W(\omega_k) \Delta\omega \quad (4)$$

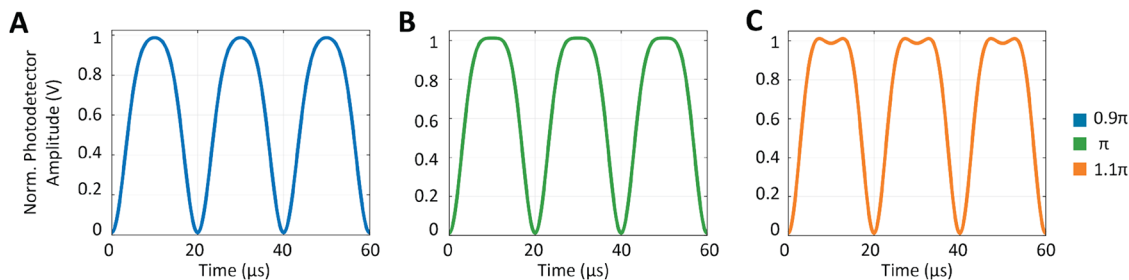


Figure 2. Cross-polarizer calibration method. The output signal of the cross-polarizer calibration method is shown for different PEM retardance values: (A) below 0.5 or equivalently below phase of π (B) at 0.5 or equivalently phase of π (C) above 0.5 or equivalently above phase of π .

Sample Preparation

For the acquisition of VCD data, α -pinene samples were prepared at varying enantiomeric excess (0, 0.25, 0.5, 0.75, and 1) by mixing commercially available (+)- α -pinene and (-)- α -pinene (Sigma-Aldrich, purity >98%). Approximately 14 μL of each sample were transferred to a custom-built, mid-IR-transparent barium fluoride (BaF_2) cell with a path length of 100 μm . The cell was sealed to prevent evaporation during the measurement process. All samples were prepared and handled under ambient conditions. The optical densities (OD) of the samples in the spectral region of interest (1000–1300 cm^{-1}) were confirmed to be between 0.4 and 1.0 to optimize the SNR of the acquired VCD spectra. Prior to measurements, the system was calibrated using a low-stress plate to correct for any phase discrepancies in the setup.

RESULTS AND DISCUSSION

We have developed a VCD spectrometer capable of subminute spectral acquisition, as shown schematically in Figure 1. The system incorporates a high-sensitivity mercury cadmium telluride (MCT) detector, optimized for the mid-infrared (IR) range (5.7–10 μm) with low noise characteristics, making it ideal for capturing inherently weak VCD signals from chiral molecules. Photoelastic modulators play a pivotal role in chiral sensing, enabling the generation of alternating circularly polarized (CP) light states required for accurate VCD measurements. Traditionally, PEMs in VCD systems operate at a fixed frequency, often not spectrally matched to the operating wavenumber. This mismatch leads to inefficiencies due to the inherent chromatic behavior of PEMs, which typically exhibit optimal performance at discrete spectral frequencies. Chromatic variations across the operating wavenumber range can deviate by 10–20% from the nominal value,³¹ significantly impacting the generation of CP light, especially in broadband applications. These discrepancies, along with deviations between set and actual retardance values, necessitate careful calibration to achieve accurate performance.

PEM Integration and Calibration

PEM Synchronization with Pulsed QCL. Many calibration methodologies rely on calibrating the modulator at a specific retardance and wavelength, then mathematically extending these results to other retardances and wavelengths. One widely used technique for calibrating a PEM is the cross-polarizer method.⁴⁶ This approach employs a setup comprising of a polarizer (P_0), PEM, analyzer (P_θ), and a photovoltaic mercury cadmium telluride (PV-MCT) detector. A high-speed data acquisition (DAQ) card captures the amplitude-modulated signal, and Welch's method is used to extract the DC and second harmonic ($2f$) frequency components from the measured time series data. For calibration, the second polarizer

is either rotated from 0° to 360° or fixed at 90° from the first polarizer.

The setup can be mathematically represented by Stokes–Mueller matrix formalism⁴⁷ as the product of several matrices corresponding to the optical elements, as shown in eq 5.⁴⁸

$$I_{T,\text{CAL}}(\lambda, t) = M_D \cdot M_P(90^\circ) \cdot M_{\text{PEM}}(45^\circ, [\alpha_m(\lambda)]) \cdot S_0 \quad (5)$$

$$\alpha_m(\lambda) = \alpha_0(\lambda) \cdot \sin(\omega_{\text{PEM}} t) \quad (6)$$

$$= (1 \ 0 \ 0 \ 0) \cdot \begin{pmatrix} 0.5 & -0.5 & 0 & 0 \\ -0.5 & 0.5 & 0 & 0 \\ 0 & 0 & 0 & 0 \\ 0 & 0 & 0 & 0 \end{pmatrix}. \quad (7)$$

$$\begin{pmatrix} 1 & 0 & 0 & 0 \\ 0 & \cos[\alpha_m(\lambda)] & 0 & -\sin[\alpha_m(\lambda)] \\ 0 & 0 & 1 & 0 \\ 0 & \sin[\alpha_m(\lambda)] & 0 & \cos[\alpha_m(\lambda)] \end{pmatrix} \cdot \frac{I_0(\lambda)}{2} \begin{pmatrix} 1 \\ 0 \\ 0 \\ 0 \end{pmatrix}$$

$$= \frac{I_0(\lambda)}{4} (1 - \cos[\alpha_0(\lambda) \sin(\omega_{\text{PEM}} t)])$$

(7)

$I_T(\lambda)$ is the total intensity recorded by the detector after it transmits through the optical system at the wavelength, λ . M_D denotes a simplified detector, $M_P(90^\circ)$ denotes a polarizer oriented at 90° , and $S_0(\lambda)$ denotes an unpolarized light source after passing through a 0° polarizer. $M_{\text{PEM}}(45^\circ, [\alpha_m(\lambda)])$ represents a photoelastic modulator oriented at 45° to its fast axis, modulated sinusoidally based on the wavelength dependent retardance $\alpha_0(\lambda)$, and PEM resonant frequency, $\omega_{\text{PEM}} = 2\pi f_{\text{PEM}}$.

For a continuous source (nonpulsed laser), the output described in eq 7 can be easily observed on an oscilloscope. When the PEM retardance phase, α_0 , equals π or an integral multiple of π , the signal exhibits a flat top. When $\alpha_0(\lambda) \sin(\omega_{\text{PEM}} t)$ oscillates around $-\pi$ and $+\pi$, the slope of the sinusoidal term is minimized causing the flat peaks seen in Figure 2B. Conversely, when the retardance phase is less than π , the cosine function displays more pronounced peaks, shown in Figure 2A. This occurs because the sinusoidal term $\sin(\omega_{\text{PEM}} t)$ has its steepest slope near zero, causing rapid changes in the input to the cosine function. If the retardance

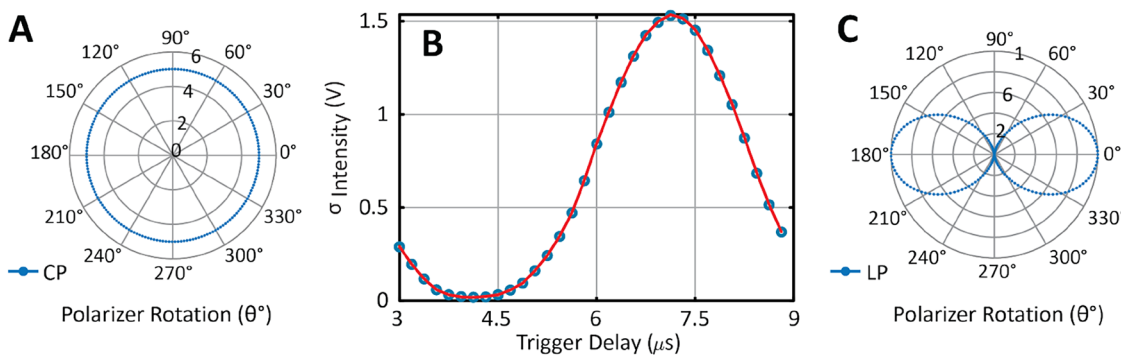


Figure 3. (A) Voltage data for CP light as a function of analyzer polarizer angle. (B) Standard deviation of recorded voltage vs QCL trigger delay, identifying the optimal delay for PEM synchronization. (C) Voltage data for linear polarization as a function of analyzer polarizer angle.

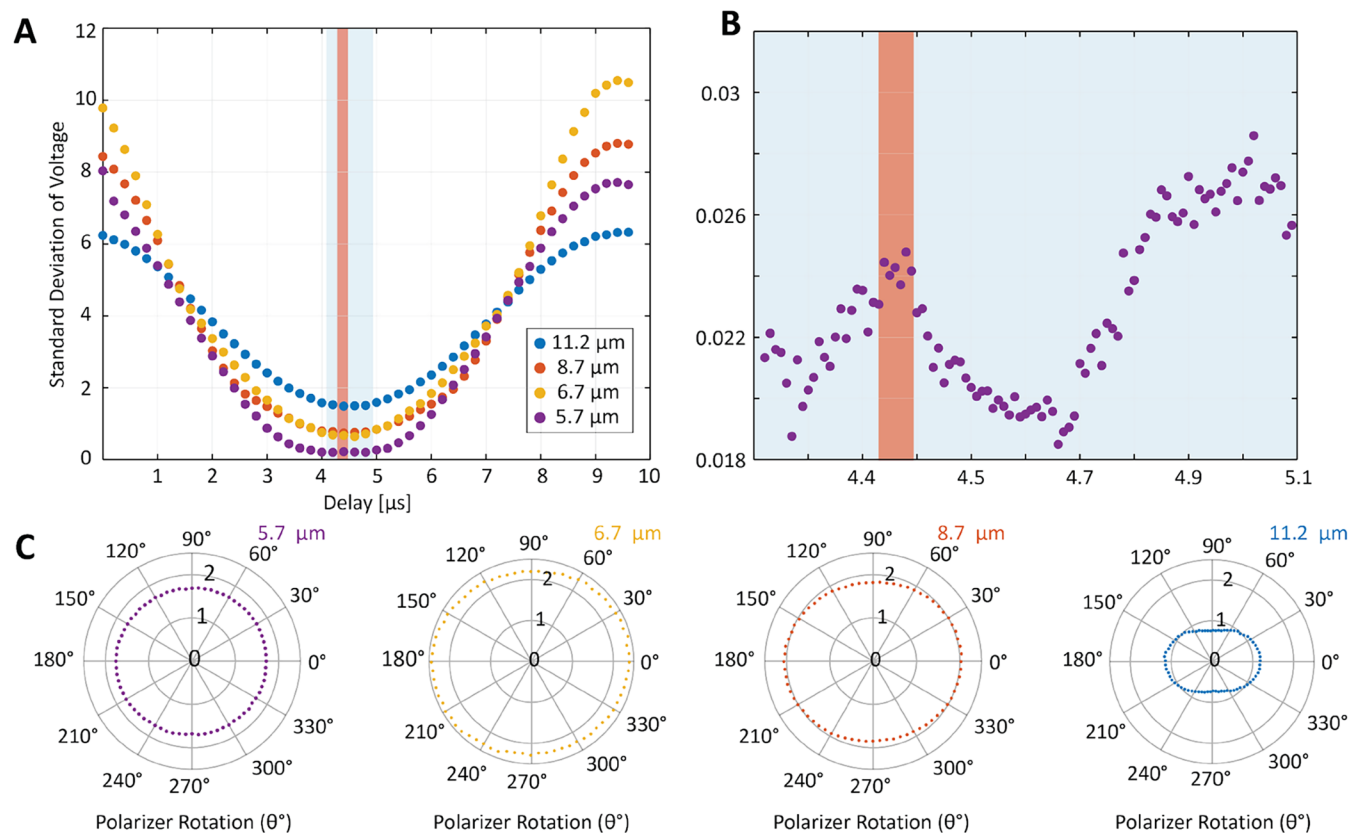


Figure 4. (A) Standard deviation of intensity as a function of QCL trigger delay for the center wavelengths of QCL chips. (B) Zoomed-in view showing the optimized delay of 4.45 μs . (C) Measured voltage as a function of polarizer angle for representative wavelengths using the optimized delay of 4.45 μs .

phase exceeds π , a dip appears in the middle of the peak, illustrated in Figure 2C, indicating that the cosine has surpassed $\pm\pi$. Using this method, the voltage for π retardance can be calibrated within 1–2% accuracy.⁴⁶ The applied voltage scales linearly with the PEM's retardance, allowing the voltage value for one retardance at one wavelength to be scaled to other retardances at the same wavelength using eq 8.

$$V_a(\lambda) = \frac{\alpha}{\pi} V_\pi(\lambda) \quad (8)$$

The applied voltage is proportional to wavelength and the voltage corresponding to that same retardance over a range of wavelengths can be found using eq 9 below. Applying voltage to the PEM results in a strain given by gV where g is the gain applied via stress. t_z is the thickness of the PEM modulation

material and $C(\lambda)$ is the stress-optical coefficient as a function of wavelength.⁴⁹

$$V_a(\lambda) = \frac{\alpha}{2\pi g t_z} \frac{\lambda}{C(\lambda)} \quad (9)$$

The PEM's modulation varies sinusoidally, peaking at a specified retardance, and any trigger delay between the PEM and the laser alters the output polarization. Consequently, the laser trigger must be synchronized such that the laser pulses align with the PEM's peak retardance, as shown in Figure 1A. To ensure synchronization between the laser and the PEM, a calibration method outlined is implemented, with a rotating polarizer before the detector. For each delay, the pulse intensity is measured as the rotating polarizer varies from 0° to

360°, and the standard deviation of the data is calculated. The PEM is set to peak at a quarter-wave phase shift, so when the QCL pulses align with the 0.25λ retardance, the output light becomes circular. As a result, due to the polarization-insensitive nature of the detector, the intensity at the photodetector does not vary with the polarizer angle, as seen in Figure 3A, and the standard deviation is minimized. Conversely, the standard deviation is maximized when the polarization is linear, as seen in Figure 3C. A QCL was used, featuring individual chips that cover subsections of its wavelength range between 5 and 10 μm . The plots in Figure 4A illustrate the variation in standard deviation for the center wavelengths of different QCL chips. As expected, the phase delay value remains consistent across all the chips, and thus, across the entire spectral range of interest. However, since the retardance is set to 0.25λ without prior calibration, discrepancies arise at certain wavelengths. As seen in Figure 4A, the lower wavelength chip centered at 5.7 μm is slightly above 0.25λ , whereas the chips at higher wavelengths fall below 0.25λ . Synchronization revealed an optimum delay, $\Delta\Phi_{\text{opt}}$, of 4.45 μs across the spectral range (Figure 4). The measured detector voltage as a function of polarizer angle was then plotted for the representative wavelengths with an optimized delay of 4.45 μs in Figure 4C. Residual linear polarization was observed for 6.7 and 8.7 μm wavelengths, with significant contribution at 11.2 μm highlighting the need for further PEM retardance calibration.

PEM Retardance Calibration Using Bessel Fitting. The PEM can be modulated from zero to 1λ at lower wavelengths and from zero to a value less than 1λ at higher wavelengths. This modulation is based on a factory calibration, which is only accurate for the 0.5λ value. As a result, the PEM needs to be recalibrated to determine the factory retardance values that correspond to 0.25λ . The PEM retardance was varied from 0 to its maximum value per wavelength, for wavelengths between 5.7 and 10 μm . The voltage time series data was collected.

The setup can be modeled by eq 5 and further expanded using DC and second order Bessel functions as shown in eq 10 where α_{cal} is the newly calibrated PEM retardance. The DC and $2\omega_{\text{PEM}}(2f)$ power components (varying with PEM retardance) can be fitted to eq 10, multiplied by a fitted parameter to convert intensity to power.

$$I_{T,\text{CAL}}(\lambda) = \frac{I_0(\lambda)}{4}(1 - J_0[\alpha_{\text{cal}}(\lambda)]) - \frac{I_0(\lambda)}{4}(2J_2[\alpha_{\text{cal}}(\lambda)]) \sin(2\omega_{\text{PEM}}t) \quad (10)$$

However, since this measurement is taken before calibrating the PEM's retardance, the actual retardance may vary. This leads to the data shown in Figure 5. If the PEM's peak retardance is below 0.25λ , the output polarization is elliptical, and the minimum standard deviation is higher. If the PEM's peak retardance is above 0.25λ , the output polarization remains elliptical but passes through 0.25λ retardance, resulting in a curve that first reaches a minimum, then increases slightly before returning to a second minimum.

Next, the PEM can be calibrated for 0.25λ retardance. The ratio of the DC and second order Bessel components between two retardances—one known and one unknown—can be used to accurately determine the unknown retardance. From the oscilloscope method, the 0.5λ calibration is known to be accurate within 1–2%. As a result, the intensity at the PEM

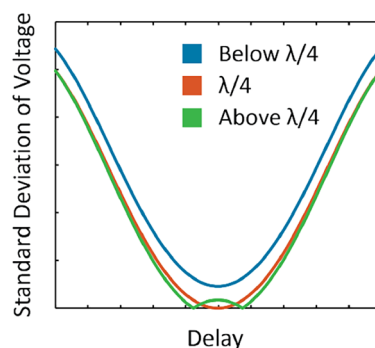


Figure 5. Standard deviation analysis for PEM retardance calibration. Standard deviation of voltage as a function of QCL trigger delay, showing the optimal delay when the PEM retardance is below, at, or above quarter-wave shift.

factory calibrated retardance 0.5λ is used in eqs 11 and 12 to find the intensity at 0.25λ .

$$I_{\text{DC}}\left[\frac{\lambda}{4}\right] = \frac{1 - J_0(\pi/2)}{1 - J_0(\pi)} I_{\text{DC}}\left[\frac{\lambda}{2}\right] = 0.4048 \cdot I_{\text{DC}}\left[\frac{\lambda}{2}\right] \quad (11)$$

With the intensity at 0.5λ known, the intensity at 0.25λ can be estimated as

$$I_{2f}\left[\frac{\lambda}{4}\right] = \frac{J_2(\pi/2)}{J_2(\pi)} I_{2f}\left[\frac{\lambda}{2}\right] = 0.5144 \cdot I_{2f}\left[\frac{\lambda}{2}\right] \quad (12)$$

With the new intensity value for 0.25λ retardance, the corresponding PEM factory retardance is determined by the DC and $2f$ power data. To calibrate the PEM, we measure the intensity of the transmitted light as a function of the set maximum wave retardance (δ_M) for four representative QCL wavelengths: 5.7, 6.7, 8.7, and 9.7 μm , where the phase retardance, $\alpha = \delta \times 2\pi$, where, δ is the wave retardance. These measurements capture the modulation behavior of the PEM under varying conditions and help determine the actual retardance values corresponding to the nominal settings. The recorded intensity values are fitted to second-order Bessel functions using eq 12, where the fitting parameters characterize the retardance profile for each wavelength. Solid lines in Figure 6A represent the best-fit curves through the experimental data points. These fits allow for precise determination of the retardance values at different wavelengths, accounting for the chromatic variation inherent in PEM operation. The calibrated PEM retardance as a function of the QCL-incident wavelength is shown in Figure 6B. The results indicate a wavelength-dependent deviation from the set retardance, with chromatic variations of up to 8–12% from the nominal value. This highlights the necessity for wavelength-specific calibration techniques to achieve accurate modulation of CP light across the mid-infrared range.

QCL-VCD Spectrometer Performance and Characterization

α -Pinene (\pm) QCL-VCD Spectra. With precise acquisition of LCP and RCP light states across the entire spectral regime of interest, we turn our focus to the VCD spectra of (\pm)- α -pinene, a bicyclic monoterpene, and a widely recognized standard in VCD systems. α -Pinene exhibits distinct VCD signatures, making it an exemplary benchmark for evaluating VCD spectrometer performance. The IR absorbance and VCD spectra of (\pm)- α -pinene were measured using the QCL-VCD spectrometer, focusing on the mid-infrared range. The IR

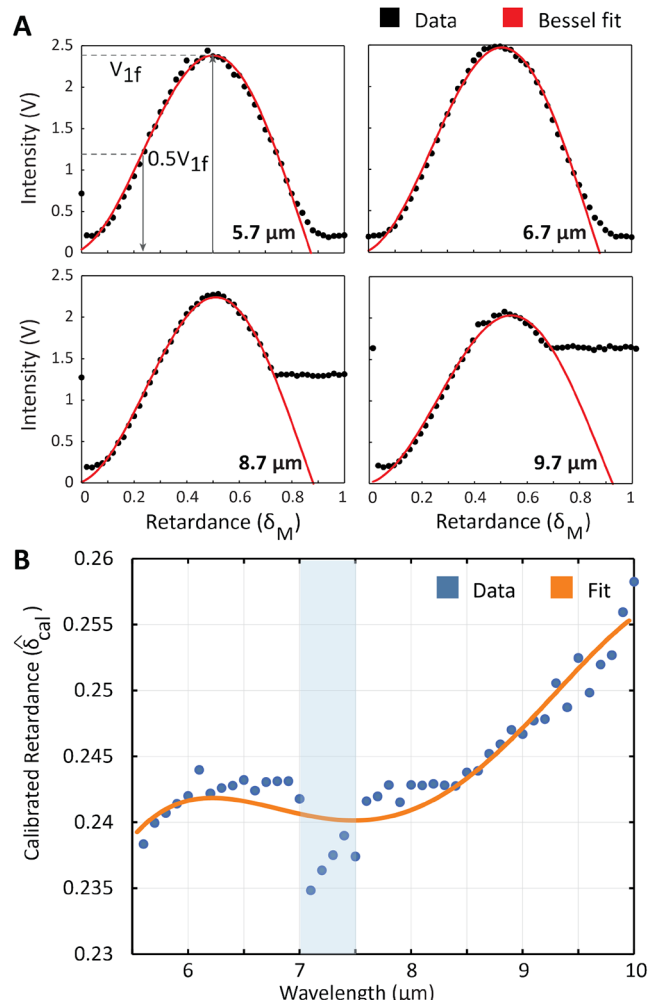


Figure 6. PEM retardance characterization and calibration. (A) Recorded intensity vs set maximum retardance (δ_M) with corresponding Bessel function fits for four representative QCL-chips wavelengths, namely, 5.7, 6.7, 8.7, and 9.7 μm . The solid lines through the data points are best fits using eq 12 with the corresponding fitting parameters for second order Bessel function (B) calibrated PEM retardance, $\hat{\delta}_{\text{cal}}$ as a function of the QCL-incident wavelength. Due to the low SNR observed between 7 and 7.5 μm , the data within this range is not considered statistically reliable.

absorbance spectra (Figure 7B) clearly show characteristic vibrational modes of α -pinene. The VCD spectra (Figure 7A) were acquired between 1000 and 1300 cm^{-1} with a resolution of 2 cm^{-1} .

α -Pinene (\pm) Enantiomeric Excess Determination. A key analytical application of VCD spectroscopy is determining the optical purity of a chiral sample. This is quantified using enantiomeric excess,⁵¹ a measure of the relative abundance of one enantiomer over the other. The enantiomeric excess (*e.e.*) is defined as +1 for pure α -pinene (+), 0 for racemic mixture and -1 for pure α -pinene (-). To evaluate the relationship between enantiomeric excess and VCD spectral features, five samples with enantiomeric excess ranging from -1 to 1 were prepared volumetrically in steps of 0.5 by adjusting the concentration of (+)- α -pinene in the mixture. The VCD spectra of these mixtures are shown in Figure 8A. While conventional infrared absorption spectroscopy produced identical spectra for all samples, demonstrating its inability to differentiate enantiomers, VCD spectra distinctly revealed the

optical purity of each sample. A linear regression analysis was performed to examine the correlation between enantiomeric excess and the VCD peak values and is shown in Figure 8C. High correlation coefficients ($R > 0.99$) were obtained for all selected bands, indicating a strong linear relationship between enantiomeric excess and VCD signal intensity across the spectral region. Statistical analysis validated the precision and reliability of these measurements. These results highlight the robustness of QCL-VCD spectroscopy for accurate quantification of enantiomeric excess, providing valuable insights for applications in chiral analysis.

We observe distinct VCD peaks for (-)- α -pinene at 1062, 1101, 1125, 1166, 1181, 1202, 1216, 1232, 1244, and 1262 cm^{-1} , closely corresponding to values reported in FT-VCD literature^{50,52} (see Supporting Table S2). Notably, our experimental spectra show strong agreement in both peak positions and ΔA sign assignments for several key bands, including 1126 and 1202 cm^{-1} . However, we also observe discrepancies in relative intensity, particularly for the 1099 cm^{-1} band. These variations are likely due to QCL pulse-to-pulse amplitude fluctuations, chip transition regions below 1030 cm^{-1} , and differences in detection methodology between our digitizer-based system and conventional lock-in-based FT-VCD instruments. To support reproducibility and transparent benchmarking, we include a complete peak-by-peak comparison in Table S2, along with labeled spectra in Figure S2. These results demonstrate that our QCL-VCD system can acquire high-quality spectra of chiral small molecules such as α -pinene within subminute time scales, with performance comparable to established FT-VCD systems. Although any VCD band with reasonable SNR can be used, the bands with the maxima at 1202 cm^{-1} are presented. The SNR for the measurements, particularly at the 1202 cm^{-1} peak, was calculated for multiple measurements, demonstrating the reproducibility and reliability of the system. The consistency of the measured VCD data and SNR as a function of number of measurements (Figure 8C) indicates sufficient time stability and sensitivity of the entire experimental setup. Variations in peak positions may arise due to differences in conformational states, sample preparation, path length, sample thickness, or optical effects from the spectrometer's condensing optics.⁵³ These effects contribute to inhomogeneous broadening and altered line shapes. Future improvements should integrate calibration techniques to systematically address these factors, enhancing the accuracy of VCD spectra for chiral molecules.

Further, polarization effects and instrumental artifacts can influence the observed deviations.³¹ Detailed polarization analysis using individual Mueller matrix representations could provide deeper insights into the optical system's behavior.^{54,55} Established methods for mitigating instrumental polarization effects, commonly applied in astronomy,^{56–58} may be incorporated into future system advancements. These findings emphasize the need for further refinement of QCL-VCD systems and comprehensive theoretical modeling to achieve quantitative measurements validated against ab initio calculations.

It is worth noting that the VCD spectrum corresponding to the racemic mixture (*e.e.* of 0) does not exhibit a completely flat baseline as theoretically expected. This deviation is not due to sample preparation or selective postprocessing, as all spectra in Figure 8 were uniformly processed using only a Savitzky-Golay smoothing filter without additional baseline correction. The observed low-amplitude, nonzero ΔA signal in the racemic

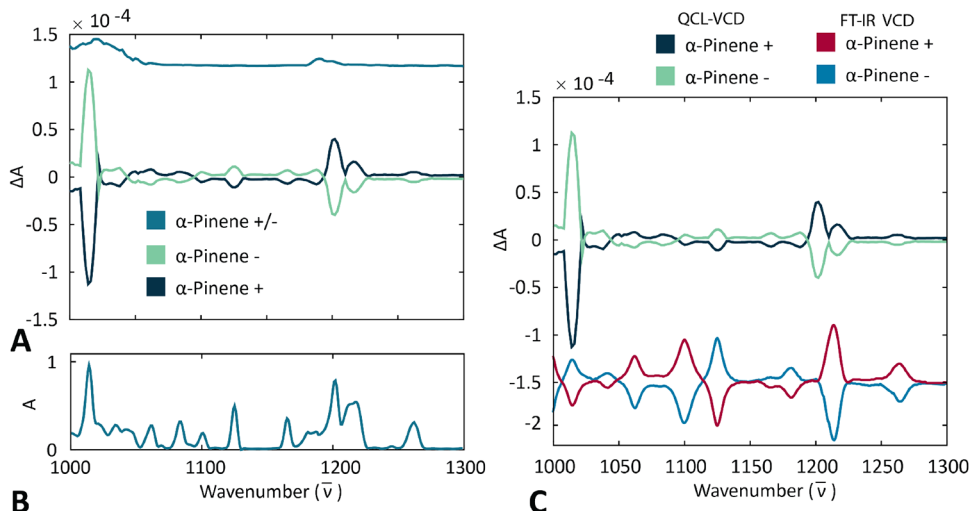


Figure 7. Pinene IR absorbance and VCD spectra. (A) α -pinene (\pm) VCD spectra has been acquired between 1000 and 1300 cm^{-1} at 2 cm^{-1} . The noise spectra ordinate is offset and shown in the panel above the spectra. (B) Racemic α -pinene \pm IR absorbance spectra acquired on the QCL-VCD spectrometer. (C) Comparison of QCL-VCD spectra of neat liquid α -pinene enantiomers (\pm) with FT-IR VCD reference spectra reported in literature.⁵⁰ The reference spectra for neat liquid α -pinene (\pm) was reproduced in part with permission from ref 50. Copyright 1997 American Chemical Society.

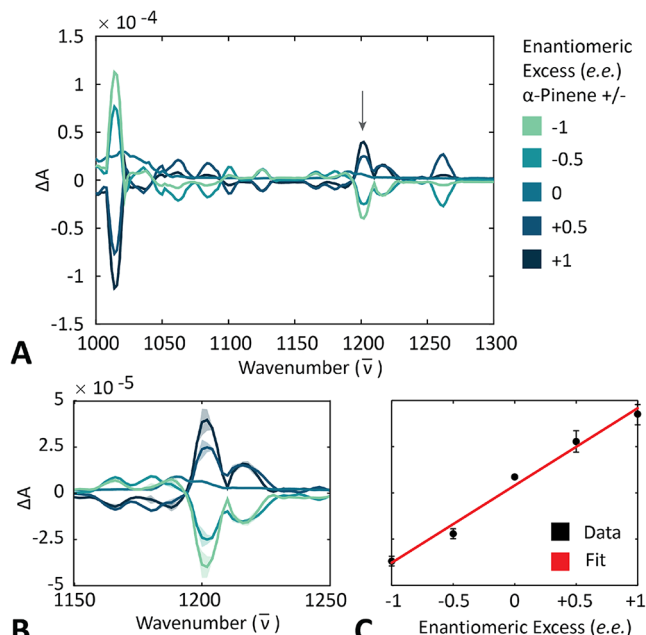


Figure 8. Pinene enantiomeric excess determination with VCD spectral acquisition. (A) α -pinene (\pm) enantiomeric excess from -1 to $+1$ in steps of 0.5 by increasing the concentration of α -pinene (+) in the mixture as acquired on the QCL-VCD spectrometer. α -pinene (\pm) VCD spectra has been acquired between 1000 and 1300 cm^{-1} at 2 cm^{-1} . The corresponding VCD spectra are obtained and calculated as the standard deviation of 20 repeated measurements. (B) The $\pm 3\sigma$ standard deviation in the VCD spectra presents 99.7% confidence level in the measurements. (C) Enantiomeric excess and VCD ΔA variation plotted at 1202 cm^{-1} alongwith the standard deviation in the measurements. Note that the enantiomeric excess data set was acquired at 2 cm^{-1} .

sample likely stems from cumulative system noise, low-frequency drifts, and detector-level fluctuations—factors that become more pronounced in measurements where the true chiroptical signal approaches zero. We have confirmed that such deviations do not correlate with analyte-specific spectral

features and instead reflect the expected limitations of signal-to-noise performance under cancellation-dominated conditions.

Data Processing Workflow and Acquisition Timing.

For VCD spectra acquisition, we record data spanning the 1000–1300 cm^{-1} range with 1 cm^{-1} resolution. Each VCD measurement encompasses 300 spectral data points, with the timing for a single left-circularly polarized (LCP) and right-circularly polarized (RCP) pulse pair being approximately 20 μs . Notably, for time-resolved studies focused on single wavelength acquisition (e.g., a spectral peak), one such 20 μs acquisition may suffice, creating the opportunity for microsecond time-scale VCD measurements in arrangements where the signal is sufficiently strong. The total acquisition time per VCD spectrum acquisition is approximately 12 s, considering 0.04 s per spectral data point. Additionally, around 200 ms is allocated for laser tuning, stabilization, and spectral tuning of the PEM, bringing the total acquisition time per spectrum to \sim 18 s. To ensure statistical repeatability and reproducibility, we perform 20 consecutive measurements per wavenumber for enantiomeric excess, resulting in a full VCD spectrum acquisition across the 1000–1300 cm^{-1} range in approximately 2 min, as illustrated in Figure 8. For noise reduction, the acquired VCD spectral data are processed using a second-order polynomial Savitzky–Golay finite impulse response (FIR) smoothing filter with a quadratic polynomial and a frame length of 8. This smoothing approach results in an effective spectral resolution of approximately 8 cm^{-1} . While the filter preserves broad spectral features, we acknowledge it may introduce minor artifacts such as peak broadening and ringing, which were taken into account during spectral interpretation.⁵⁹ This approach, combined with the system's enhanced SNR and reduced integration times, facilitates accurate and efficient enantiomeric excess measurements of VCD signals. Lastly, VCD signals are inherently bisignate, whereas absorbance signals are strictly positive. To ensure accurate data interpretation, phase correction of the instrument is essential. For this purpose, we employ a low-stress calibration plate to characterize and correct any phase discrepancies in the system.

Workflow: Timing Acquisition for VCD Spectrum Measurement Algorithmic Representation

Algorithm 1 Timing Acquisition Workflow

```

1: Initialize: Set up QCL, PEM, and measurement parameters.
2: Set range: 1000–1300 cm-1 (300 cm-1 span).
3: Select Resolution:
4: if Resolution = 1 cm-1 then
5:   Spectral bands = 300.
6:   for each band do
7:     Acquire data (0.04 s) and settle (0.02 s).
8:   end for
9:   Total: 0.06 × 300 = 18 s per spectrum.
10:  Repeat 20 times for enantiomer analysis.
11: else[Resolution = 2 cm-1]
12:   Spectral bands = 150.
13:   for each band do
14:     Acquire data (0.8 s).
15:   end for
16:   Total: 0.8×150 = 120 s per spectrum (2 minutes).
17: end if

```

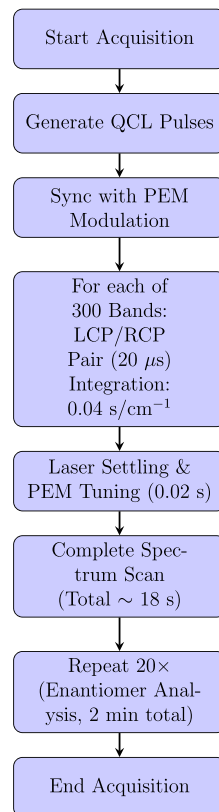


Figure 9. Timing acquisition process for VCD measurements. Side-by-side visualization of the VCD acquisition process: Left-hand side panel shows the algorithmic workflow outlining the sequential steps in timing and data acquisition, while the right-hand side panel presents the corresponding block diagram illustrating hardware coordination and synchronization for each stage.

This calibration step ensures the proper alignment of VCD signals, eliminating artifacts and enabling reliable analysis.

The digitized intensity time series is processed using Welch's method to extract power spectral density (PSD) components. This technique partitions the signal into overlapping segments, applies a window function, computes a periodogram for each segment, and averages these to reduce variance. Unlike traditional lock-in amplifiers, Welch's method enables posthoc frequency component extraction from noisy time-domain data, including the f_{QCL} and $f_{\text{QCL}} - f_{\text{PEM}}$ components specific to pulsed-laser VCD systems. To address the timing considerations of our acquisition system and clarify the signal processing pipeline, we have now included a schematic overview as well as an algorithmic workflow in Algorithmic Representation (Figure 9). This figure illustrates the sequential timing of QCL pulses, the synchronization with PEM modulation, and the windowed spectral analysis using Welch's method. Each wavenumber measurement involves 300 spectral acquisitions, with an LCP and RCP pulse pair requiring approximately 20 μ s. An additional 20 ms accounts for laser settling and PEM spectral tuning, resulting in \sim 18 s per wavenumber scan. The consistency of the measured VCD data and SNR as a function of number of measurements (Figure 8C) demonstrates sufficient time stability and sensitivity of the spectrometer. Although minor fluctuations are observed, they fall within expected statistical variation due to random noise and laser power fluctuations. Importantly, the same sample was measured repeatedly inside a 100 μ m BaF₂ cell without

repositioning, and no drift or systematic variation in spectral features was observed. These results support the stability of the setup for rapid and repeatable VCD measurements.

CONCLUSIONS

This study demonstrates a QCL-VCD system that achieves significant improvements in acquisition speed, SNR, and precision. By integrating a PEM with a pulsed QCL source and employing advanced calibration and optical configurations, the system enables accurate and rapid chiral analysis. Our system leverages hardware-based lock-in detection using Welch's method instead of traditional lock-in amplifiers, enabling real-time demodulation of the VCD signal at the difference frequency. The characterization of α -pinene mixtures validates the system's reliability and potential for high-throughput applications. Moving forward, we envision adapting this architecture for broadband or chip-tuned QCL systems to access regions $>$ 1300 cm⁻¹, including amide I and II bands. Further improvements will focus on real-time phase detection, automated baseline correction, and polarization compensation. Looking ahead, this platform offers promising prospects for the VCD analysis of complex biomolecules, including proteins, enabling insights into their secondary structures and chiral dynamics. Such advancements could pave the way for broader applications in structural biology, pharmaceutical development, and real-time biosensing technologies. These developments position QCL-VCD systems as a critical tool for next-generation molecular spectroscopy.

■ ASSOCIATED CONTENT

Data Availability Statement

The data sets generated and analyzed during this study, including processed spectral data and analysis scripts, are available from the corresponding author upon reasonable request. Raw instrument output may also be shared for collaborative purposes or verification of findings. Some components of the experimental setup and software are currently under consideration for intellectual property protection by Mines; therefore, certain details may be limited in disclosure.

§ Supporting Information

The Supporting Information is available free of charge at <https://pubs.acs.org/doi/10.1021/acsmmeasureau.5c00069>.

Comparison of acquisition times for VCD spectra across this work and prior FT-IR and QCL-based studies (Table S1); calculated timing estimates based on reported scan parameters, lock-in settings, and averaging schemes; detailed comparison of experimental VCD peak positions and ΔA sign assignments for $(-)\alpha$ -pinene, aligned against literature-reported FT-VCD data (Table S2); additionally, annotated spectral plots highlighting band positions and relative intensities (Figures S1 and S2) to facilitate direct visual comparison and benchmark reproducibility ([PDF](#))

■ AUTHOR INFORMATION

Corresponding Author

Yamuna Phal — Department of Electrical Engineering, Colorado School of Mines, Golden, Colorado 80401, United States; Quantitative Biosciences and Engineering Program, Colorado School of Mines, Golden, Colorado 80401, United States; Colorado Clinical & Translational Sciences Institute (CCTS), Aurora, Colorado 80045, United States;
✉ orcid.org/0000-0002-2602-7012; Email: yphal@mines.edu

Authors

Viviana Arrunategui Norwick — Department of Electrical Engineering, Colorado School of Mines, Golden, Colorado 80401, United States

Michael Le — Department of Electrical Engineering, Colorado School of Mines, Golden, Colorado 80401, United States

Eric Modesitt — Department of Computer Science, University of Illinois Urbana-Champaign, Urbana-Champaign, Illinois 61801, United States

Owen Myers — Department of Electrical Engineering, Colorado School of Mines, Golden, Colorado 80401, United States

Roya Akrami — Department of Electrical Engineering, Colorado School of Mines, Golden, Colorado 80401, United States

Complete contact information is available at:
<https://pubs.acs.org/10.1021/acsmmeasureau.5c00069>

Notes

The authors declare no competing financial interest.

■ ACKNOWLEDGMENTS

This material is based upon work supported in part by the National Science Foundation Partnership for Innovation Program via Grant No. 2414684 and the National Aeronautics and Space Administration PICASSO program via Grant No. 23-PICASSO23-0026. Viviana appreciates the support provided by Clare Booth Luce Fellowship.

■ REFERENCES

- (1) Brown, J. M.; Davies, S. G. Chemical asymmetric synthesis. *Nature* **1989**, *342*, 631–636.
- (2) Nguyen, L. A.; He, H.; Pham-Huy, C. Chiral drugs: An overview. *Int. J. Biomed. Sci.* **2006**, *2*, 85–100.
- (3) Calcaterra, A.; D'Acquarica, I. The market of chiral drugs: Chiral switches versus de novo enantiomerically pure compounds. *J. Pharm. Biomed. Anal.* **2018**, *147*, 323–340.
- (4) Vargesson, N. Thalidomide-induced teratogenesis: History and mechanisms. *Birth Defects Res., Part C* **2015**, *105*, 140–156.
- (5) Tokunaga, E.; Yamamoto, T.; Ito, E.; Shibata, N. Understanding the Thalidomide Chirality in Biological Processes by the Self-disproportionation of Enantiomers. *Sci. Rep.* **2018**, *8*, No. 17131.
- (6) Vargesson, N. Thalidomide-induced teratogenesis: History and Mechanisms. *Birth Defects Res., Part C* **2015**, *105*, 140–156.
- (7) Stephens, P. J.; Lowe, M. Vibrational circular dichroism. *Annu. Rev. Phys. Chem.* **1985**, *36*, 213–241.
- (8) Stephens, P. J. Gauge dependence of vibrational magnetic dipole transition moments and rotational strengths. *J. Phys. Chem. A* **1987**, *91*, 1712–1715.
- (9) Shah, R.; Nafie, L. Spectroscopic methods for determining enantiomeric purity and absolute configuration in chiral pharmaceutical molecules. *Curr. Opin. Drug Discovery Dev.* **2001**, *4*, 764–775.
- (10) Freedman, T.; Cao, X.; Nafie, L.; Solladié-Cavallo, A.; Jierry, L.; Bouerat, L. VCD configuration of enantiopure/-enriched tetrasubstituted α -fluoro cyclohexanones and their use for epoxidation of trans-olefins. *Chirality* **2004**, *16*, 467–474.
- (11) Nafie, L. A.; Dukor, R. K. Applications of Vibrational Optical Activity in the Pharmaceutical Industry. In *Handbook of Vibrational Spectroscopy*; John Wiley & Sons, 2006; Vol. 1.
- (12) Nafie, L. A.; Keiderling, T.; Stephens, P. Vibrational circular dichroism. *J. Am. Chem. Soc.* **1976**, *98*, 2715–2723.
- (13) Nafie, L. A.; Diem, M.; Vidrine, D. W. Fourier transform infrared vibrational circular dichroism. *J. Am. Chem. Soc.* **1979**, *101*, 496–498.
- (14) Ragunathan, N.; Lee, N.; Freedman, T.; Nafie, L.; Tripp, C.; Buijs, H. Measurement of vibrational circular dichroism using a polarizing Michelson interferometer. *Appl. Spectrosc.* **1990**, *44*, 5–7.
- (15) Nafie, L. A.; Buijs, H.; Rilling, A.; Cao, X.; Dukor, R. K. Dual source Fourier transform polarization modulation spectroscopy: An improved method for the measurement of circular and linear dichroism. *Appl. Spectrosc.* **2004**, *58*, 647–654.
- (16) Guo, C.; Shah, R. D.; Dukor, R. K.; Cao, X.; Freedman, T. B.; Nafie, L. A. Determination of enantiomeric excess in samples of chiral molecules using Fourier transform vibrational circular dichroism spectroscopy: Simulation of real-time reaction monitoring. *Anal. Chem.* **2004**, *76*, 6956–6966.
- (17) Stephens, P. J. Theory of vibrational circular dichroism. *J. Phys. Chem. A* **1985**, *89*, 748–752.
- (18) Devlin, F. J.; Stephens, P.; Cheeseman, J.; Frisch, M. Ab initio prediction of vibrational absorption and circular dichroism spectra of chiral natural products using density functional theory: camphor and fenchone. *J. Phys. Chem. A* **1997**, *101*, 6322–6333.
- (19) Nafie, L. A.; Freedman, T. B. Vibronic coupling theory of infrared vibrational transitions. *J. Chem. Phys.* **1983**, *78*, 7108–7116.
- (20) Mayerhöfer, T. G.; Singh, A. K.; Huang, J.-S.; Krafft, C.; Popp, J. Unveiling chiral optical constants of α -pinene and propylene oxide through ATR and VCD spectroscopy in the mid-infrared range. *Spectrochim. Acta, Part A* **2023**, *302*, No. 123136.

- (21) Keiderling, T. A. Protein and peptide secondary structure and conformational determination with vibrational circular dichroism. *Curr. Opin. Chem. Biol.* **2002**, *6*, 682–688.
- (22) Polavarapu, P. L.; He, J. Peer Reviewed: Chiral Analysis Using Mid-IR Vibrational CD Spectroscopy. *Anal. Chem.* **2004**, *76*, 61A–67A.
- (23) Shanmugam, G.; Polavarapu, P. L. Vibrational circular dichroism of protein films. *J. Am. Chem. Soc.* **2004**, *126*, 10292–10295.
- (24) Shanmugam, G.; Polavarapu, P. L. Film techniques for vibrational circular dichroism measurements. *Appl. Spectrosc.* **2005**, *59*, 673–681.
- (25) Keiderling, T. A.; Lakhani, A. Conformational studies of biopolymers, peptides, proteins, and nucleic acids. A role for vibrational circular dichroism. *Compr. Chiropt. Spectrosc.* **2012**, *2*, 707–758.
- (26) Keiderling, T. A. Instrumentation for Vibrational Circular Dichroism Spectroscopy: Method Comparison and Newer Developments. *Molecules* **2018**, *23*, No. 2404.
- (27) Keiderling, T. A. Structure of Condensed Phase Peptides: Insights from Vibrational Circular Dichroism and Raman Optical Activity Techniques. *Chem. Rev.* **2020**, *120*, 3381–3419.
- (28) Nafie, L. A.; Guo, C.; Dukor, R. K. Reaction Monitoring of Chiral Molecules Using Fourier Transform Infrared Vibrational Circular Dichroism Spectroscopy. U.S. Patent, US7,378,283, 2008.
- (29) Nafie, L. A. Instrumentation for Vibrational Circular Dichroism. In *Vibrational Optical Activity: Principles and Applications*; John Wiley & Sons, Chapter 6, 2011.
- (30) Nafie, L. A. Vibrational Optical Activity: From Discovery and Development to Future Challenges. *Chirality* **2020**, *32*, 667–692.
- (31) Phal, Y.; Yeh, K.; Bhargava, R. Concurrent Vibrational Circular Dichroism Measurements with Infrared Spectroscopic Imaging. *Anal. Chem.* **2021**, *93*, 1294–1303.
- (32) Sato, H.; Shimizu, M.; Watanabe, K.; Yoshida, J.; Kawamura, I.; Koshoubu, J. Multidimensional Vibrational Circular Dichroism Apparatus Equipped with Quantum Cascade Laser and Its Use for Investigating Some Peptide Systems Containing d-Amino Acids. *Anal. Chem.* **2021**, *93*, 2742–2748.
- (33) Sato, H.; Yamagishi, A.; Shimizu, M.; Watanabe, K.; Koshoubu, J.; Yoshida, J.; Kawamura, I. Mapping of Supramolecular Chirality in Insect Wings by Microscopic Vibrational Circular Dichroism Spectroscopy: Heterogeneity in Protein Distribution. *J. Phys. Chem. Lett.* **2021**, *12*, 7733–7737.
- (34) Hermann, D. R.; Ramer, G.; Kitzler-Zeiler, M.; Lendl, B. Quantum cascade laser-based vibrational circular dichroism augmented by a balanced detection scheme. *Anal. Chem.* **2022**, *94*, 10384–10390.
- (35) Phal, Y.; Yeh, K.; Bhargava, R. Design Considerations for Discrete Frequency Infrared Microscopy Systems. *Appl. Spectrosc.* **2021**, *75*, 1067–1092.
- (36) Phal, Y.; Pfister, L.; Carney, P. S.; Bhargava, R. Resolution Limit in Infrared Chemical Imaging. *J. Phys. Chem. C* **2022**, *126*, 9777–9783, DOI: 10.1021/acs.jpcc.2c00740.
- (37) Kemp, J. C. Piezo-Optical Birefringence Modulators: New Use for a Long-Known Effect. *J. Opt. Soc. Am.* **1969**, *59*, 950–954.
- (38) Wang, B.; List, J. In *Basic Optical Properties of the Photoelastic Modulator: Part I. Useful Aperture and Acceptance Angle*, Proceedings of SPIE—The International Society for Optical Engineering; SPIE, 2005; p 1.
- (39) Liu, D.; Liu, N.; Zhou, S.; Li, J. Comparison of digital lock-in amplifier and fast fourier transform algorithms for quartz-tuning-fork enhanced spectroscopy. *Opt. Quantum Electron.* **2020**, *52*, No. 417.
- (40) Chen, R.; Zhu, C.; Ge, B.; Zhu, X.; Sun, Y.-S.; Mi, L.; Ma, J.; Wang, X.; Fei, Y. Detecting Signals With Direct Fast Fourier Transform for Microarray Data Collection. *IEEE Photonics Technol. Lett.* **2017**, *29*, 2211–2214.
- (41) Mei, L.; Svanberg, S. Wavelength modulation spectroscopy—digital detection of gas absorption harmonics based on Fourier analysis. *Appl. Opt.* **2015**, *54*, 2234–2243.
- (42) Fernholz, T.; Teichert, H.; Ebert, V. Digital, phase-sensitive detection for *in situ* diode-laser spectroscopy under rapidly changing transmission conditions. *Appl. Phys. B: Laser Opt.* **2002**, *75*, 229–236.
- (43) Solomon, O. M., Jr *PSD Computations Using Welch's Method*, NASA STI/Recon Technical Report N; Sandia National Laboratories, 1991.
- (44) Ruppert, M. G.; Harcombe, D. M.; Ragazzon, M. R.; Moheimani, S. R.; Fleming, A. J. A review of demodulation techniques for amplitude-modulation atomic force microscopy. *Beilstein J. Nanotechnol.* **2017**, *8*, 1407–1426.
- (45) Welch, P. The use of fast Fourier transform for the estimation of power spectra: a method based on time averaging over short, modified periodograms. *IEEE Trans. Audio Electroacoust.* **1967**, *15*, 70–73.
- (46) Oakberg, T. *PEM 200 Photoelastic Modulator User Manual*; Hinds Instruments Inc., 2020; p 1.
- (47) Goldstein, D. H. *Polarized Light, Revised, and Expanded*; CRC Press, 2003.
- (48) Nafie, L. A.; Dukor, R. K.; Freedman, T. B. *Handbook of Vibrational Spectroscopy*; John Wiley & Sons, Ltd, 2006.
- (49) Sutherland, J. C. Calibration of photoelastic modulator based dichrometers: maintaining constant phase across the spectrum. *J. Instrum.* **2016**, *11*, No. P07016.
- (50) Devlin, F. J.; Stephens, P. J.; Cheeseman, J. R.; Frisch, M. J. Ab Initio Prediction of Vibrational Absorption and Circular Dichroism Spectra of Chiral Natural Products Using Density Functional Theory: α -Pinene. *J. Phys. Chem. A* **1997**, *101*, 9912–9924.
- (51) Nafie, L. A.; Freedman, T. B. Vibrational circular dichroism: an incisive tool for stereochemical applications. *Enantiomer* **1998**, *3*, 283–297.
- (52) Urbanová, M.; Setnička, V.; Volka, K. Measurements of concentration dependence and enantiomeric purity of terpene solutions as a test of a new commercial VCD spectrometer. *Chirality* **2000**, *12*, 199–203.
- (53) Nafie, L. A. Dual polarization modulation: a real-time, spectral-multiplex separation of circular dichroism from linear birefringence spectral intensities. *Appl. Spectrosc.* **2000**, *54*, 1634–1645.
- (54) Berry, H. G.; Gabrielse, G.; Livingston, A. Measurement of the Stokes parameters of light. *Appl. Opt.* **1977**, *16*, 3200–3205.
- (55) Schaefer, B.; Collett, E.; Smyth, R.; Barrett, D.; Fraher, B. Measuring the Stokes polarization parameters. *Am. J. Phys.* **2007**, *75*, 163–168.
- (56) Tinbergen, J. Accurate Optical Polarimetry on the Nasmyth Platform. *Publ. Astron. Soc. Pac.* **2007**, *119*, 1371–1384.
- (57) Norris, B.; Schworer, G.; Tuthill, P.; Jovanovic, N.; Guyon, O.; Stewart, P.; Martinache, F. The VAMPIRES instrument: Imaging the innermost regions of protoplanetary discs with polarimetric interferometry. *Mon. Not. R. Astron. Soc.* **2015**, *447*, 2894–2906.
- (58) Jäger, F. W. Instrumental polarization concerning magnetographic measurements. *Sol. Phys.* **1972**, *27*, 481–488.
- (59) Schmid, M.; Rath, D.; Diebold, U. Why and how Savitzky-Golay filters should be replaced. *ACS Meas. Sci. Au* **2022**, *2*, 185–196.